NANO LETTERS

pubs.acs.org/NanoLett

Letter

Ergodic and Nonergodic Dynamics of Oxygen Vacancy Migration at the Nanoscale in Inorganic Perovskites

Omur E. Dagdeviren,* Aaron Mascaro, Shuaishuai Yuan, Javad Shirani, Kirk H. Bevan, and Peter Grütter*

Cite This: *Nano Lett.* 2020, 20, 7530−7535

Read Online

ACCESS | Metrics & More | Article Recommendations | Supporting Information

ABSTRACT: Perovskites are widely utilized either as a primary component or as a substrate in which the dynamics of charged oxygen vacancy defects play an important role. Current knowledge regarding the dynamics of vacancy mobility in perovskites is solely based upon volume- and/or time-averaged measurements. This impedes our understanding of the basic physical principles governing defect migration in inorganic materials. Here, we measure the ergodic and nonergodic dynamics of vacancy migration at the relevant spatial and temporal scales using time-resolved atomic force microscopy techniques. Our findings demonstrate that the time constant associated with oxygen vacancy migration is a local property and can change drastically on short length and time scales, such that nonergodic states lead to a dramatic increase in the migration barrier. This correlated spatial and temporal variation in oxygen vacancy dynamics can extend hundreds of nanometers across the surface in inorganic perovskites.

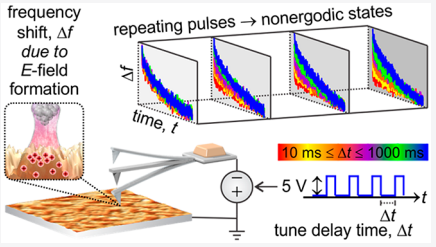

KEYWORDS: *Perovskites, strontium titanate, oxygen vacancy migration, atomic force microscopy, time-resolved atomic force microscopy, charge carrier dynamics*

Charge carriers (i.e., electrons, holes, vacancies, ions, etc.) and their interaction with the surrounding host lattice have an extraordinary impact on the properties of materials. Due to their widespread scientific and technological use, measuring oxygen vacancy migration within perovskite-based systems has been a long-term effort.[1,2] Experimentally, it was found that surface phases can alter migration barriers.[3,4] The concentration of charge carriers, which couple directly with oxygen vacancy dynamics, can also be tuned with an external electric field or through mechanical modification.[5−9] Importantly, oxygen concentration changes across the surface can in turn modify oxygen dynamics and incorporation.[4] Theoretically, it has been postulated that oxygen vacancies can cluster, thereby resulting in local oxygen vacancy migration barrier variability.[10] Recently, it has been demonstrated that the motion of atoms at the atomic scale can be measured and even manipulated, via intriguing in situ transmission electron microscopy methods.[11,12] However, existing probe-based measurements of oxygen migration dynamics are macroscopically volume- and/or time-averaged at scales that are orders of magnitude larger than the governing physical dimensions (e.g., nanometers and milliseconds).[1,3−5,7−9,13,14] Such macroscopic averaging is a fundamental problem in experimental physics and nonequilibrium thermodynamics, as it obscures a deeper understanding of the basic atomic-scale principles that govern the diffusive dynamics of charge carriers. This is true not only for oxygen migration in perovskites but also for charge carriers in many other systems including two-dimensional van der Waals heterostructures.[15−19]

Here, we report the ergodic (i.e., history-independent) and nonergodic (i.e., history-dependent) dynamics of charge carriers at the nanometer length scale. A single crystal of $SrTiO_3$ was utilized in our experiments (see section I of our Supporting Information). The use of a single crystal minimizes sample property variations that may exist in many perovskite films.[2] The insulating nature of our samples and our ab initio calculations indicate that +2 charge state oxygen vacancies are the dominant charge carriers within our sample system (see sections I and VI of our Supporting Information). As Figure 1a summarizes, the charge density and projected density of states plots show that the single neutral oxygen vacancy (V_O) is a double donor with one electron trapped in the oxygen vacancy site and the other electron delocalized in the conduction band. This is in good agreement with results obtained via hybrid functional calculations.[20] Figure 1b reveals that the charge state V_O^+ in $SrTiO_3$ leaves an extra electron trapped in the vacancy site, while, as presented in Figure 1c, V_O^{2+} only distorts the lattice around the vacancy site. Thermodynamically, the formation energy of these three defect variations depends on the electron density and thereby the overall conductivity of $SrTiO_3$. At low electronic conductivity (i.e., low electron

Received: July 21, 2020
Revised: September 23, 2020
Published: September 24, 2020

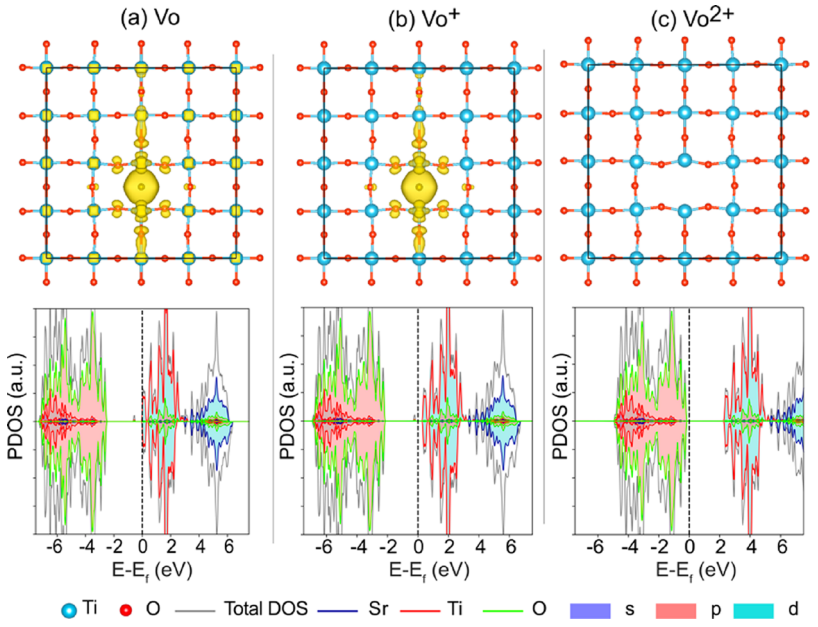

Figure 1. The upper row depicts charge density contributions (yellowish cloud) and lattice distortions resulting from single oxygen vacancies. The lower row provides the projected density of states with the elemental resolved electronic structure for (a) Vo, (b) Vo^{+}, and (c) Vo^{2+} in $SrTiO_3$, respectively.

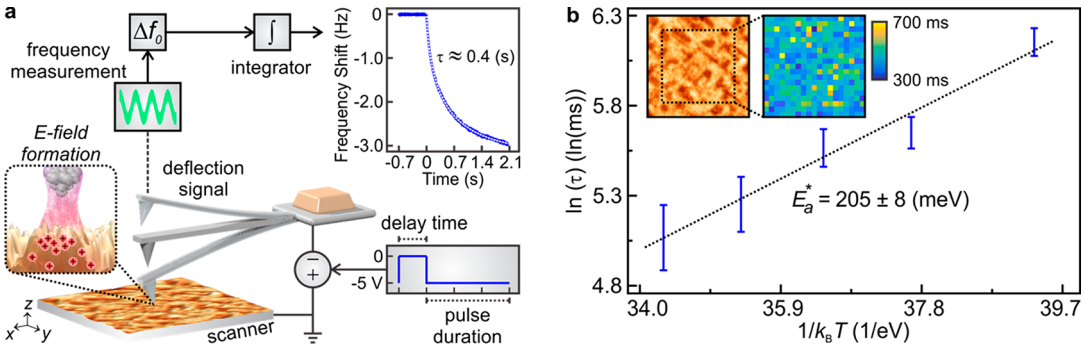

Figure 2. Schematic explanation of the experimental flow and the local measurement of oxygen vacancy migration time constants as a function of temperature. (a) A bias voltage is applied between the tip and the sample. The applied bias voltage introduces a time-dependent Coulomb interaction between the cantilever and the sample. This additional force results in a resonance frequency shift, Δf_0, which is demodulated. The procedure is repeated, and the results of different measurements on the same spatial position are integrated to enhance the measurement accuracy (see section III of our Supporting Information for details). The time-dependent frequency shift data is used to extract the dynamics of oxygen vacancy migration, i.e., time constant (τ), and associated energy barriers for their movement (see section II of our Supporting Information for details). (b) The slope of the Arrhenius plot of the natural logarithm of the time constant (in ms) vs $1/(k_BT)$, where k_B is the Boltzmann constant and T is the temperature in Kelvin, discloses the effective activation energy of oxygen vacancies.[21] The vertical bars show the variation of the time constant across the surface within an area of 500 nm × 500 nm. The inset shows the topography of the sample and the region that we conducted time constant measurements at room temperature (see section IV of our Supporting Information and Figure S3).

densities), the formation of V_O^{2+} vacancies is strongly favored, as discussed in ref 20 and also reproduced in our Supporting Information. As our samples display extremely low electronic conductivity, theoretical calculations indicate that the samples should be dominated primarily by V_O^{2+} vacancies (see section VI of our Supporting Information for details concerning these first-principles calculations).

We measured the dynamic properties of oxygen vacancy migration by employing a recently developed, time-resolved, high-resolution scanning probe microscopy technique[21] (see section II of our Supporting Information). As Figure 2a summarizes, an electric field was applied between a sharp probe tip and the sample. The step-change in the electric field leads to a large instantaneous capacitive, attractive electrostatic tip−sample interaction. Mobile charges in the sample screen the external field, leading to a decay in the tip−sample interaction reflecting the sample's charge dynamics (Figure 2a). This time-dependent variation in force on the tip can be measured by demodulating the cantilever's resonance frequency. For our sample, we find an exponential decay in tip−sample force with a characteristic time constant of several 100 ms (Figure 2a). We repeated the experiment at each spatial position to enhance the signal-to-noise ratio and measured the time constant of charge carriers with less than 2% uncertainty (see section III of our Supporting Information and Figure S1). Repeating these experiments at the same location and the same tip−sample separation requires a very stable and low-drift microscope with an active drift compensation.

https://dx.doi.org/10.1021/acs.nanolett.0c03002
Nano Lett. 2020, 20, 7530−7535

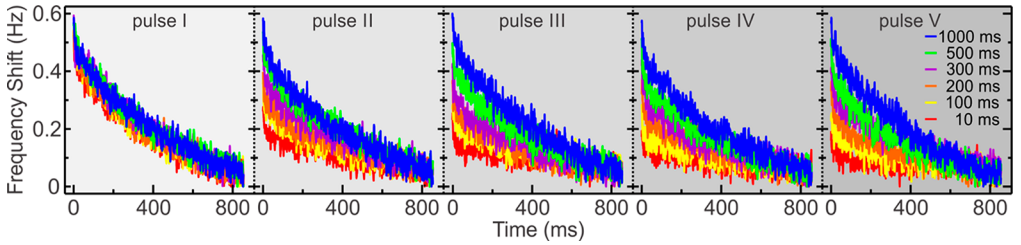

Figure 3. Measurement of the time constant of oxygen vacancy migration with different delay times between pulses. With an increasing number of pulses, the effect of nonergodic states becomes evident. All of the first pulses (pulse I) show the same decay time, demonstrating that we are measuring at the same sample location. We separately show the response to the second, third, fourth, and fifth pulse in a pulse train (pulse II to pulse V), with a color-coded delay time between the individual pulses in a pulse train ranging from 10 to 1000 ms.

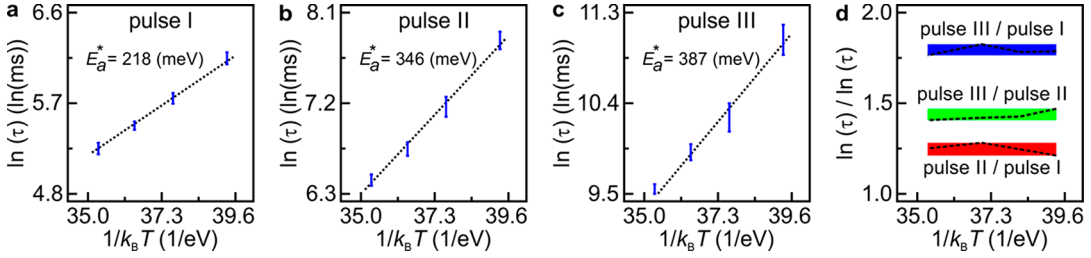

Figure 4. Measurement of ergodic and nonergodic state activation barrier. (a) The activation barrier of the unperturbed system is 218 meV. (b, c) The activation barrier of the nonergodic system is measured with a delay time of 10 ms between pulses. (d) The ratio of the logarithm of the time constants is nearly constant with respect to inverse temperature.

We measured the near equilibrium, i.e., ergodic, time constant of charge carrier migration on a grid of 20 × 20 with 25 nm spacings as a function of temperature (Figure 2b). Our results reveal that the time constant of charge carriers is a local sample property that evolves with surface structure and the local surface stoichiometry (e.g., possibly local surface termination and distance from step edges) and can change by a factor of 2 on a nanometer length scale (see section IV of the Supporting Information and Figure S3 for details). In Figure 2b, the vertical error bars are not a measurement error but rather show the variation across the surface (see section III of the Supporting Information and Figure S1). The measured effective activation energy, E_a*, of the equilibrium state charge carriers is 205 ± 8 meV, which is smaller than the volume- and time-averaged macroscopic measurements (~0.6 eV for nominally undoped $SrTiO_3$).[1] This equilibrium effective state activation energy results in a single-ion bulk-phase activation energy of 180 ± 12 meV and an effective attempt rate of 10^{-6} s (see section II of our Supporting Information). Our experiments reveal that the attempt rate of oxygen vacancies is significantly lower than the attempt rate of ionic movement measured in battery materials. This lower attempt rate may be linked to the size of oxygen vacancies and their strong interaction with the lattice structure.[21]

The ergodic effective activation barrier can be reproducibly measured if we wait long enough until the system reaches equilibrium. However, we observed that the measured activation barrier depends on how much the sample is perturbed away from equilibrium, when one measures the barrier along a nonergodic diffusion pathway. Specifically, we applied the electric field pulse between the sample and the scanned probe with different time delays between successive pulses while remaining at the same spatial position through active drift control (see section II of our Supporting Information and Figure 2a). Figure 3 shows that nonergodic, temporally correlated effects become evident with successive pulses. If pulses are spaced 1 s apart, all of the decay times are the same. Meaning, after 1 s of delay, the system always returns to the same (ergodic) state. Surprisingly, we observe that the decay time constant (τ) of subsequent pulses becomes longer as the delay time between pulses decreases. This is most easily seen for a sequence of pulses; e.g., the response to the fifth pulse shows the strongest increase in τ as a function of decreasing pulse delay times. We interpret this striking observation as follows. For the first pulse, the time constant associated with the motion of charge carriers is the same (the system started in equilibrium), demonstrating that the tip−sample position was held constant. However, if the delay time between individual pulses is less than the time required for the relaxation of oxygen vacancies (=equilibration time), about 1 s for $SrTiO_3$, the decay time constant increases monotonically (see also Figure S4 for additional data).

To further quantify the observed temporal correlations, we measured the nonergodic effective activation energy of charge carriers for a fixed 10 ms delay between pulses. We conducted nonergodic activation barrier measurements away from step edges on flat regions of the sample to avoid complication of the data interpretation due to possible screening effects by step edges (though this is likely to be negligible for the large screening lengths under consideration, due to the low conductivity of our samples). As Figure 4 shows, the effective activation energy of the first pulse is 218 meV at the measured location; surprisingly, it increases monotonically for the second (346 meV) and third pulses (387 meV) at the same sample location. This increase in the effective activation barrier also leads to an increase in the single-ion bulk-phase activation energy, which is measured as 181 meV for the first pulse and increases gradually for the second (270 meV) and third pulses (288 meV). These rising migration barrier trends are consistent with our complementary ab initio calculations (see sections VI and VII of our Supporting Information), which propose that the change in the effective activation is linked to

https://dx.doi.org/10.1021/acs.nanolett.0c03002
Nano Lett. 2020, 20, 7530−7535

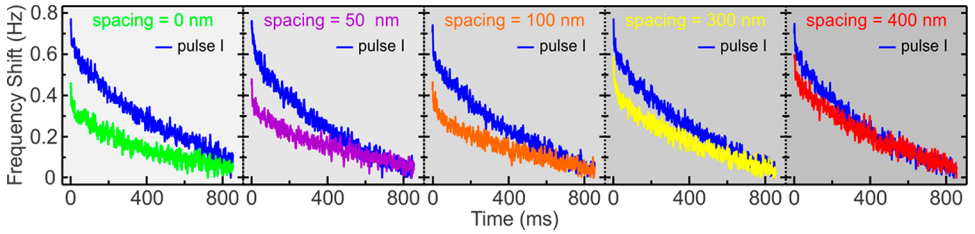

Figure 5. Measurements of the spatial extent of nonergodic dynamics. The distance between the successive pulses is increased while keeping the delay time between successive pulses constant (=50 ms). It can be seen that temporal correlations can extend hundreds of nanometers and decrease with increasing distance.

the local clustering of oxygen vacancies due to the externally applied electric field from the scanning probe. More specifically, our calculations show that the migration barrier of +2 charge state oxygen vacancies depends on the distance and orientation of paired vacancies (see sections VI and VII of our Supporting Information). We propose that, among the statistical ensemble of possible configurations that are occupied in vacancy migration, similar interactions obstruct vacancy motion and result in a larger overall migration barrier at higher vacancy concentrations. These vacancies that are initially dilute for the ergodic state can be clustered closely together in a nonergodic configuration due to the externally applied field. Although it is not possible to compute all such interactions and kinetic barriers, our calculations lend first-principles support to our hypothesis and are complementary to the observed experimental results.

The ratio of the time constants between different pulses is nearly the same and independent of temperature (see Figure 4d). This implies that even with increasing temperature the system does not relax to the equilibrium state due to the short delay time between pulses. Another important observation is that the ratio of time constants between the second and third pulses is larger than the ratio between the second and first pulses. We hypothesize that these further nonergodic increases in the time constant are therefore a consequence of cumulative charge accumulation arising from extended perturbation of the sample.

Our results highlight that the activation barrier of the ergodic state is significantly lower than the nonergodic state. This demonstrable difference between the activation barrier of ergodic and nonergodic states directly impacts the validity of conventional macroscopic time-averaged measurements of charge carrier dynamics. Our results clearly demonstrate that the measured physical quantities can be affected by the ergodicity or nonergodicity of the measurement itself within relevant time scales. Hence, time-averaged measurements may lead to a misinterpretation of the short-time-scale correlations within materials associated with charge carrier dynamics. To this end, our results demonstrate that care should be taken when analyzing macroscopic time-averaged measurements, as they mainly reflect the charge carrier dynamics of the ergodic system, which has a lower effective activation barrier compared to the nonergodic sample system. Correspondingly, the defect diffusion rate and mobility decrease with an increase in the nonergodic activation barrier (see section VIII of our Supporting Information). For this reason, our nonergodic findings regarding charge carrier dynamics are particularly relevant with respect to inherently nonequilibrium energy and quantum technologies, which rely heavily upon engineering the mobility of charge carriers.[22]

We further investigated the spatial extent of nonergodic states by changing the spatial location between individual pulses while keeping the delay time constant (=50 ms). As Figure 5 shows, the temporal correlations for a locally applied electric field can extend up to 400 nm along the lateral direction. The effect of the tip and sample modification during the experiments can be excluded (Figure S9). This long-range spatial effect can be due to either the accumulation of charge carriers or the mechanical strain induced by the oxygen vacancies and the tip−sample interaction force, which may deform the lattice.[7−9,23] More specifically, Das et al. demonstrated that tip−sample interaction forces that are in the order of μNs can be used for the controlled manipulation of oxygen vacancies using nanoscale flexoelectricity.[9] However, our noncontact scanning probe microscopy experiments measure negative frequency shifts at a distance; this results in tip−sample interaction forces that are orders of magnitude lower. Our theoretical calculations, which are based on experimental tip−sample interaction forces, show that mechanical deformation by the applied electric field between the tip and the sample can be discounted as a source of temporal correlations for such small tip−sample interaction forces (see section VI-b of our Supporting Information). For this reason, these results imply that the spatial extent of nonergodic states is electronic in origin and arises due to the accumulation of charge carriers (that may be associated with the presence of small polarons[20]). Our measurements also demonstrate that the local measurement of physical properties can be altered due to nearby measurements, which can be particularly important for point spectroscopy experiments such as on high-T_c superconductors.

In summary, a significant difference between the ergodic and nonergodic dynamics of oxygen migration has been observed at the nanoscale in $SrTiO_3$. Our experiments and complementary *ab initio* calculations show three important results. First, we experimentally demonstrated significant temporal and spatial variation in nonergodic dynamics, including defect activation energy barriers. Second, our experiments and complementary ab initio calculations reveal that nonergodic dynamics can dominate short time scale oxygen vacancy migration in such materials. More specifically, our ab initio calculations highlight that the nonequilibrium clustering of charged vacancies is likely the origin of the observed nonergodic dynamics in $SrTiO_3$. Third, we experimentally quantified the effect of nonergodic correlations on vacancy migration and their nanoscale spatial extent within the surface plane. We anticipate that our findings on the spatial and temporal variation of oxygen vacancy migration will enable a more complete understanding of the physics governing defect charge dynamics. These insights may also facilitate new

https://dx.doi.org/10.1021/acs.nanolett.0c03002
Nano Lett. 2020, 20, 7530−7535

emerging technologies relying upon tailored local vacancy mobility and engineered interactions in inorganic materials. Future scanning probe microscopy experiments capable of resolving individual defects at the atomic scale will provide invaluable insights regarding the influence of relative atomic positions on nonergodic dynamics. Finally, this methodology can be applied to a wide range of materials to illuminate the role of nonergodic phenomena on short time scales, for example, capturing the dynamics properties of moiré excitons in van der Waals heterostructures.[15−19]

■ ASSOCIATED CONTENT

Supporting Information

The Supporting Information is available free of charge at https://pubs.acs.org/doi/10.1021/acs.nanolett.0c03002.

Sample preparation; scanning probe microscopy measurements; time constant measurement accuracy; detailed analysis of surface morphology; additional experimental data for pulse experiments; first-principles calculations; first-principles methodology; relation between the activation energy and diffusion; and additional experimental data for the spatial extent of temporal correlations (PDF)

Run input files and output coordinates of DFT calculations with different convergence criteria for the ionic relaxation loop (data presented as text file) (ZIP)

■ AUTHOR INFORMATION

Corresponding Authors

Omur E. Dagdeviren − *Department of Mechanical Engineering, École de Technologie Supérieure, University of Quebec, Montreal, Quebec, Canada H3C 1K3; Department of Physics, McGill University, Montreal, Quebec, Canada H3A 2T8;* orcid.org/0000-0002-4881-9280; Email: omur.dagdeviren@etsmtl.ca

Peter Grütter − *Department of Physics, McGill University, Montreal, Quebec, Canada H3A 2T8;* orcid.org/0000-0003-1719-8239; Email: peter.grutter@mcgill.ca

Authors

Aaron Mascaro − *Department of Physics, McGill University, Montreal, Quebec, Canada H3A 2T8*

Shuaishuai Yuan − *Materials Engineering, McGill University, Montreal, Quebec, Canada H3A 0C5*

Javad Shirani − *Materials Engineering, McGill University, Montreal, Quebec, Canada H3A 0C5*

Kirk H. Bevan − *Materials Engineering, McGill University, Montreal, Quebec, Canada H3A 0C5;* orcid.org/0000-0001-9884-1403

Complete contact information is available at: https://pubs.acs.org/10.1021/acs.nanolett.0c03002

Author Contributions

O.E.D. conceived the project and conducted experiments. O.E.D. and P.G. designed the experiments and wrote the manuscript. A.M. helped O.E.D. for the initial setup of the experiment. O.E.D., S.Y., K.H.B., and P.G. planned the ab initio calculations. S.Y. performed the ab initio calculations with the help of J.S. All authors participated in the analysis and the interpretation of the data and commented on the manuscript.

Notes

The authors declare no competing financial interest.

■ ACKNOWLEDGMENTS

This work was supported by the Natural Sciences and Engineering Research Council of Canada and Le Fonds de Recherche du Québec - Nature et Technologies. S.Y. and J.S. gratefully acknowledge the McGill Engineering Doctoral Awards Program. O.E.D. gratefully acknowledges a Banting Fellowship and funds provided by École de Technologie Supérieure, University of Quebec.

■ REFERENCES

(1) De Souza, R. A. Oxygen Diffusion in $SrTiO_3$ and Related Perovskite Oxides. *Adv. Funct. Mater.* **2015**, *25* (40), 6326−6342.

(2) Leng, K.; Fu, W.; Liu, Y.; Chhowalla, M.; Loh, K. P. From bulk to molecularly thin hybrid perovskites. *Nature Reviews Materials* **2020**, *5*, 482.

(3) Tsvetkov, N.; Lu, Q.; Sun, L.; Crumlin, E. J.; Yildiz, B. Improved chemical and electrochemical stability of perovskite oxides with less reducible cations at the surface. *Nat. Mater.* **2016**, *15* (9), 1010−1016.

(4) Riva, M.; Kubicek, M.; Hao, X.; Franceschi, G.; Gerhold, S.; Schmid, M.; Hutter, H.; Fleig, J.; Franchini, C.; Yildiz, B.; Diebold, U. Influence of surface atomic structure demonstrated on oxygen incorporation mechanism at a model perovskite oxide. *Nat. Commun.* **2018**, *9* (1), 3710.

(5) Szot, K.; Speier, W.; Bihlmayer, G.; Waser, R. Switching the electrical resistance of individual dislocations in single-crystalline $SrTiO_3$. *Nat. Mater.* **2006**, *5* (4), 312−320.

(6) Kumar, A.; Ciucci, F.; Morozovska, A. N.; Kalinin, S. V.; Jesse, S. Measuring oxygen reduction/evolution reactions on the nanoscale. *Nat. Chem.* **2011**, *3* (9), 707−713.

(7) Kumar, A.; Arruda, T. M.; Kim, Y.; Ivanov, I. N.; Jesse, S.; Bark, C. W.; Bristowe, N. C.; Artacho, E.; Littlewood, P. B.; Eom, C.-B.; Kalinin, S. V. Probing Surface and Bulk Electrochemical Processes on the $LaAlO_3$−$SrTiO_3$ Interface. *ACS Nano* **2012**, *6* (5), 3841−3852.

(8) Yang, Y.; Zhang, X.; Qin, L.; Zeng, Q.; Qiu, X.; Huang, R. Probing nanoscale oxygen ion motion in memristive systems. *Nat. Commun.* **2017**, *8* (1), 15173.

(9) Das, S.; Wang, B.; Cao, Y.; Rae Cho, M.; Jae Shin, Y.; Mo Yang, S.; Wang, L.; Kim, M.; Kalinin, S. V.; Chen, L.-Q.; Noh, T. W. Controlled manipulation of oxygen vacancies using nanoscale flexoelectricity. *Nat. Commun.* **2017**, *8* (1), 615.

(10) Cuong, D. D.; Lee, B.; Choi, K. M.; Ahn, H.-S.; Han, S.; Lee, J. Oxygen Vacancy Clustering and Electron Localization in Oxygen-Deficient $SrTiO_3$:LDA+U Study. *Phys. Rev. Lett.* **2007**, *98* (11), 115503.

(11) Dyck, O.; Ziatdinov, M.; Lingerfelt, D. B.; Unocic, R. R.; Hudak, B. M.; Lupini, A. R.; Jesse, S.; Kalinin, S. V. Atom-by-atom fabrication with electron beams. *Nature Reviews Materials* **2019**, *4* (7), 497−507.

(12) Liu, Y.; Borodinov, N.; Lorenz, M.; Ahmadi, M.; Kalinin, S. V.; Ievlev, A. V.; Ovchinnikova, O. S. Hysteretic Ion Migration and Remanent Field in Metal Halide Perovskites. *Advanced Science* **2020**, 2001176.

(13) Yang, Y.; Huang, R. Probing memristive switching in nanoionic devices. *Nature Electronics* **2018**, *1* (5), 274−287.

(14) Aristidou, N.; Eames, C.; Sanchez-Molina, I.; Bu, X.; Kosco, J.; Islam, M. S.; Haque, S. A. Fast oxygen diffusion and iodide defects mediate oxygen-induced degradation of perovskite solar cells. *Nat. Commun.* **2017**, *8* (1), 15218.

(15) Urbaszek, B.; Srivastava, A. Materials in flatland twist and shine. *Nature* **2019**, *567*, 39−40.

(16) Seyler, K. L.; Rivera, P.; Yu, H.; Wilson, N. P.; Ray, E. L.; Mandrus, D. G.; Yan, J.; Yao, W.; Xu, X. Signatures of moiré-trapped valley excitons in $MoSe_2$/WSe_2 heterobilayers. *Nature* **2019**, *567* (7746), 66−70.

(17) Tran, K.; Moody, G.; Wu, F.; Lu, X.; Choi, J.; Kim, K.; Rai, A.; Sanchez, D. A.; Quan, J.; Singh, A.; Embley, J.; Zepeda, A.; Campbell, M.; Autry, T.; Taniguchi, T.; Watanabe, K.; Lu, N.; Banerjee, S. K.; Silverman, K. L.; Kim, S.; Tutuc, E.; Yang, L.; MacDonald, A. H.; Li, X. Evidence for moiré excitons in van der Waals heterostructures. *Nature* **2019**, *567* (7746), 71−75.
(18) Jin, C.; Regan, E. C.; Yan, A.; Iqbal Bakti Utama, M.; Wang, D.; Zhao, S.; Qin, Y.; Yang, S.; Zheng, Z.; Shi, S.; Watanabe, K.; Taniguchi, T.; Tongay, S.; Zettl, A.; Wang, F. Observation of moiré excitons in WSe_2/WS_2 heterostructure superlattices. *Nature* **2019**, *567* (7746), 76−80.
(19) Alexeev, E. M.; Ruiz-Tijerina, D. A.; Danovich, M.; Hamer, M. J.; Terry, D. J.; Nayak, P. K.; Ahn, S.; Pak, S.; Lee, J.; Sohn, J. I.; Molas, M. R.; Koperski, M.; Watanabe, K.; Taniguchi, T.; Novoselov, K. S.; Gorbachev, R. V.; Shin, H. S.; Fal'ko, V. I.; Tartakovskii, A. I. Resonantly hybridized excitons in moiré superlattices in van der Waals heterostructures. *Nature* **2019**, *567* (7746), 81−86.
(20) Janotti, A.; Varley, J. B.; Choi, M.; Van de Walle, C. G. Vacancies and small polarons in $SrTiO_3$. *Phys. Rev. B: Condens. Matter Mater. Phys.* **2014**, *90* (8), 085202.
(21) Mascaro, A.; Wang, Z.; Hovington, P.; Miyahara, Y.; Paolella, A.; Gariepy, V.; Feng, Z.; Enright, T.; Aiken, C.; Zaghib, K.; Bevan, K. H.; Grutter, P. Measuring Spatially Resolved Collective Ionic Transport on Lithium Battery Cathodes Using Atomic Force Microscopy. *Nano Lett.* **2017**, *17* (7), 4489−4496.
(22) Manzeli, S.; Ovchinnikov, D.; Pasquier, D.; Yazyev, O. V.; Kis, A. 2D transition metal dichalcogenides. *Nature Reviews Materials* **2017**, *2* (8), 17033.
(23) Marrocchelli, D.; Sun, L.; Yildiz, B. Dislocations in $SrTiO_3$: Easy To Reduce but Not so Fast for Oxygen Transport. *J. Am. Chem. Soc.* **2015**, *137* (14), 4735−4748.

https://dx.doi.org/10.1021/acs.nanolett.0c03002
Nano Lett. 2020, 20, 7530−7535

Supporting Information:

Ergodic and Nonergodic Dynamics of Oxygen Vacancy Migration at the Nanoscale in Inorganic Perovskites

Omur E. Dagdeviren[1,2,*], Aaron Mascaro[2], Shuaishuai Yuan[3], Javad Shirani[3], Kirk H. Bevan[3], Peter Grütter[2,*]

[1] Department of Mechanical Engineering, École de technologie supérieure, University of Quebec, Montreal, Quebec, Canada, H3C 1K3

[2] Department of Physics, McGill University, Montreal, Quebec, Canada, H3A 2T8

[3] Materials Engineering, McGill University, Montreal, Quebec, Canada, H3A 0C5

*Corresponding authors' email: omur.dagdeviren@etsmtl.ca and peter.grutter@mcgill.ca

I. Sample Preparation

All experiments were conducted using undoped, single crystal $SrTiO_3$ samples supplied by CrysTec GmbH, Germany. These samples were etched at the company using a buffered HF solution and cleaned with deionized water. We annealed samples in 1.1 atm O_2 in a furnace at 1270 K for 30 minutes to remove contaminants, plus heating up and cool down times of 1 hour each. Also, this recipe (i.e., cleaning with deionized water and annealing at 1270 K) eliminates fluorine residuals on the surface that may exist otherwise due to HF etching[1]. The sample temperature was measured with a thermocouple beneath the sample holder in the oxygen flux furnace. Following the oxygen annealing, we introduced the samples to vacuum within 10 minutes after cooling down to 470 K. We annealed the $SrTiO_3$ sample in the high vacuum (~ 10^{-7} mbar) at 400 K for 30 minutes. This annealing condition maintained a non-conducting substrate and results in atomically flat SrO and TiO_2 surface phases with no evidence of clusters of carbon contamination in the length scale and sample area that we performed our experiments[2] (*also see Section* IV *below for further discussion*).

II. Scanning Probe Microscopy Measurements

The scanning probe microscopy (SPM) experiments were conducted using a customized JSPM-5100 microscope. The microscope was equipped with a custom-made sample heater stage operating in high vacuum (~ 10^{-7} mbar). We employed gold-coated tips micro cantilevers by

OPUSTIPS (4XC-GG, tip diameter, r = 20 nm, stiffness, k = 9.0 N/m, and resonance frequency, f_0 = 150 kHz). We controlled the microscope with the GXSM control module with active drift control[3]. We used Nanosurf® EasyPLL Plus for the frequency shift detection. We modulated the microscope with the standard frequency modulation atomic force microscopy (FM-AFM) technique with self-excitation[4]. We used a peak-to-peak oscillation amplitude of 12 nm for all of our experiments.

Time-domain electrostatic force microscopy was originally developed by Schirmeisen[5] and has been successfully implemented Li^+ transport in $LiAlSiO_4$ with changing crystallinity[6-8], K^+ transport in $K_2O.2CaO.4SiO_2$ glass and Na^+ transport in $Na_2O.GeO_2$ glass[5]. The technique that we employed for our experiments is an extension of the time-domain electrostatic force microscopy using fast-detection electronics and high-frequency cantilever and has been recently implemented to measure Li^+ transport in $LiFePO_4$ with sub-millisecond accuracy[9]. Figure 2 in the main text summarizes the experimental flow that we used for our experiments. We applied a bias voltage step to the tip while the sample is grounded with a gold-coated copper electrode. Also, we made sure that the electrode connected to the sample is robust. Applying an electric field causes the charge carriers to move in response to the field as the ionic transport in solids is a vacancy mediated process which involves discrete hops from their initial sites to neighboring sites. For this reason, the motion of the charge carriers in the material results in a decay of the internal electric field, $E(t)$. This time-dependent variation in the tip-sample interaction force can be measured as the frequency shift of the cantilever. The measured frequency shift data is stored, and the measurement is repeated on the same spatial point to enhance the accuracy (*see Section* III *below for details*).

The time-dependent electrostatic force can be described by a simple exponential function on very short time scales[10]:

$$E(t) \propto \exp(-t/\tau) \quad \text{for } t < t_c \tag{1}$$

In equation 1, τ is the time constant for the individual motion of charge carriers at short time scales, and t_c is the cutoff time ($t_c \approx$ picosecond)[10]. However, the electrostatic field follows a stretched exponential decay for longer time scales[10, 11]:

$$E(t) \propto \exp(-t/\tau^*)^{\beta} \quad \text{for } t > t_c \tag{2}$$

In equation 2, β is the stretching factor and τ^* is the effective time constant that is observed for time scales larger than t_c. The motion of charge carriers is no longer random beyond the cutoff time and is influenced by the nearby ions (i.e., dispersive transport, in contrast to the diffuse

transport characteristic of electrons). This process is known as either the coupling model[10, 12] or the jump relaxation model[11]; both of them have similar conclusions for the time scale of our measurement even though they have different approaches.

The experimental, time-dependent frequency shift data is fit to equation 3 where Δf_0 is the initial frequency shift and Δf_s is the saturated frequency shift:

$$\Delta f(t) = \Delta f_0 + \Delta f_s \exp(-t/\tau^*)^{\beta} \quad (3)$$

According to the Arrhenius law[13, 14], the relaxation time constant τ^* changes with the temperature:

$$\tau^* = \tau_\infty^* \exp\left[E_a^*/(k_B T)\right] \quad (4)$$

where τ_∞^* is the effective attempt rate, E_a^* is the effective activation energy, k_B is the Boltzmann constant and T is the temperature. The time constant is then fit to equation 4 to determine the effective activation energy for the collective ion motion. The single ion hopping barrier can be recovered[12]:

$$E_a = \beta E_a^* \quad (5)$$

In equation 5, E_a is the hopping barrier for single ion motion. For this reason, it can be directly compared with the theoretical energy barrier obtained from *ab-initio* calculations[9]. Note that beta in equation (5) is not associated with the distribution of barriers commonly associated with disordered media. Our sample is a singe crystal, and the measurments are performed on a local length scale, the sample thus is essentially always ordered on this scale.

III. Time Constant Measurement Accuracy

The phase-locked-loop (PLL) limits the detection of time resolution (i.e., the fastest change in frequency) for FM-AFM measurements as PLLs typically have a finite response time. The time constant of our PLL is experimentally determined to be 20 ms[15]. We repeated the experiment at each spatial position to reach a target measurement precision. As Figure S1 demonstrates, each measurement was repeated to reach below 2% precision for the time constant measurement. We typically repeated our measurements for 20 times at each spatial position, which results in a precision better than 2%.

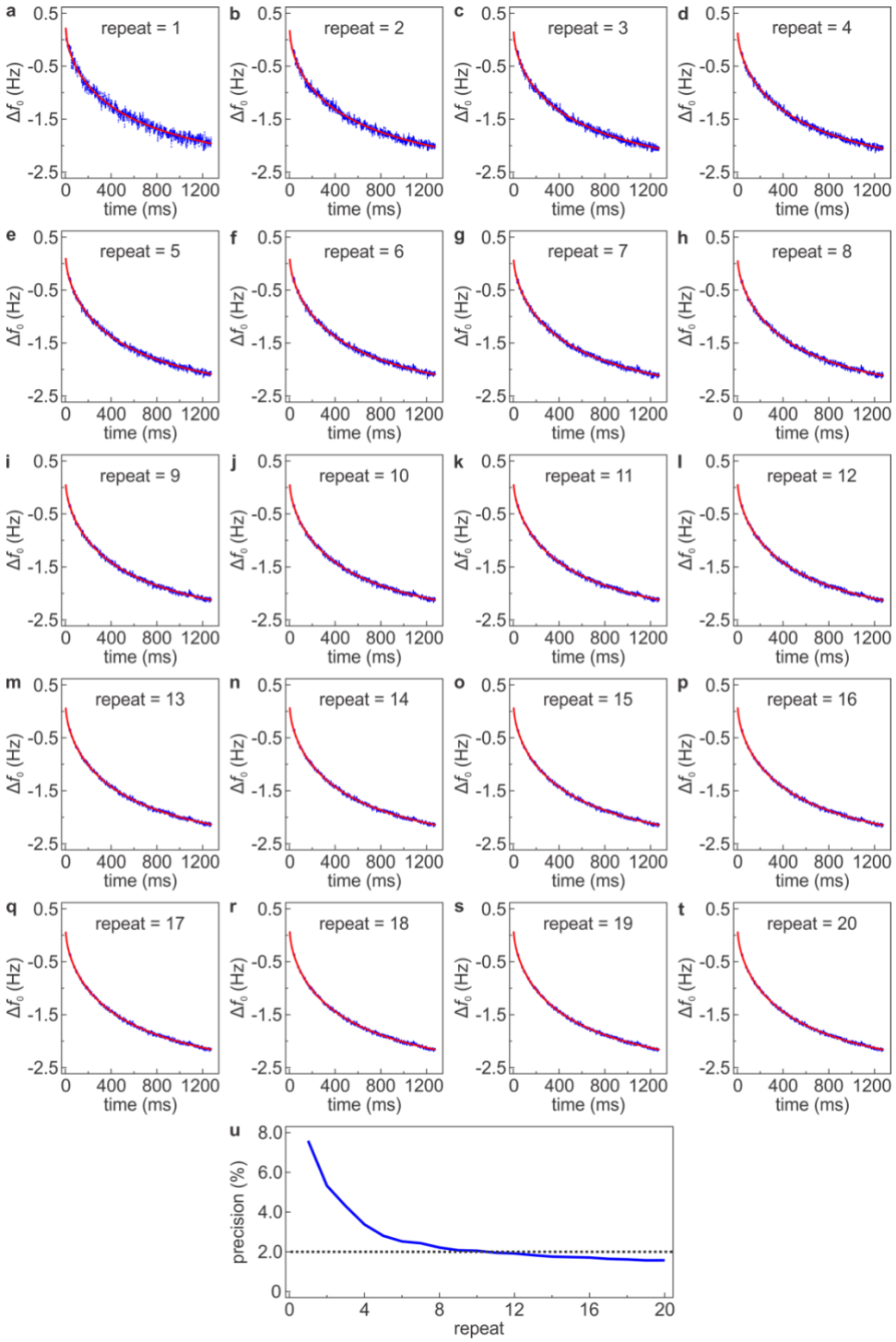

Figure S1. Variation of the precision of the time constant with the increasing number of measurements. (a-t) shows the evolution of the averaged frequency shift data up to 20 repetitions (red curve is the fit of Equation 3, and the blue curve is the experimental data). (u) displays the precision of the fit as a function of repetitions. The precision is around 8% if the experiment is conducted only once; however, with an increasing number of measurements the accuracy of the fit increases. The time constant of this measurement is determined as 508 ± 8 ms which results in a precision better than 2%.

IV. Detailed Analysis of Surface Morphology

The sample is transferred through the air and annealed up to 400K under vacuum conditions (10^{-7} mbar) for 30 minutes. Although our sample preparation recipe eliminates the large clusters of carbon and fluorine contamination, it is expected that the surface has a monolayer of adsorbates shortly after (i.e., 30 seconds). We conducted validation experiments for different materials to make sure that the recorded time-resolved response is not dominated by surface adsorbates or contaminants in the vacuum as a result of their clustering and relaxation with the applied bias voltage. As Figure S2 summarizes, we utilized single-crystal sapphire, gold, and $SrTiO_3$ samples and measured their time-dependent response under the same experimental conditions with the same probe tips. As we performed experiments for these three samples under *exactly* the same conditions, it is anticipated that if the time-dependent response is dominated by the surface adsorbates or contaminants, there will not be any measurable difference for these three samples. Our validation experiments presented in Figure S2a shows that the time-dependent response of sapphire and gold are significantly different compared to the time-dependent response of $SrTiO_3$. To cross-validate our results, we measured the time-dependent response of sapphire and gold both before (Figure S2a) and after we measured the $SrTiO_3$ sample (Figure S2b). Our control experiments on sapphire and gold show the same trend and the time constants for these samples are reproducibly and significantly different than the response of the $SrTiO_3$. Also, we want to note that the measurement of the ionic response of $LiFeO_4$ under the same vacuum conditions with the same microscope for a former work also revealed a time constant of 3 to 7 ms[9] which is different than the measured values (i.e., hundreds of milliseconds) for the $SrTiO_3$. These validation experiments endorse that the measured time-dependent response is not dominated by the monolayer adsorbates on the surface or due to the clustering and relaxation of contaminants in the vacuum.

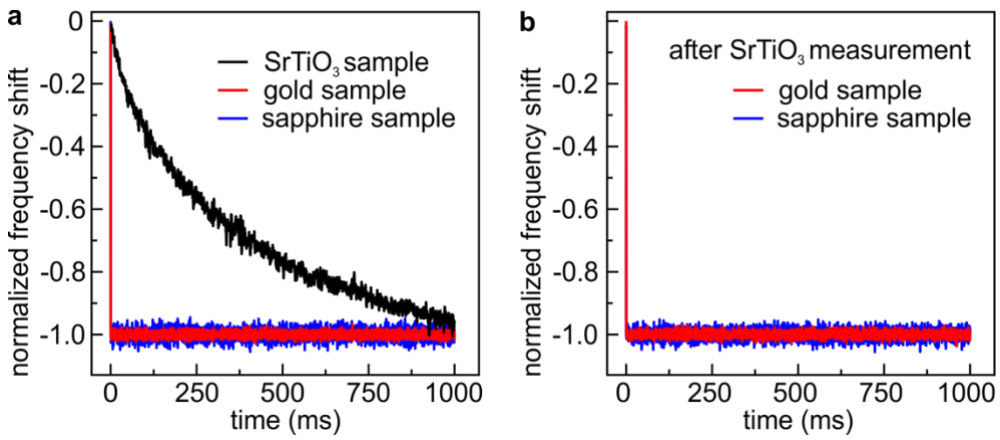

Figure S2. Response validation experiments. (a) Normalized frequency shift vs. time measurements performed on 430μm thick single-crystal sapphire, gold, and the $SrTiO_3$ under the same experimental conditions with the same probe tips. (b) We repeated the experiments on gold and sapphire after the measurement of the $SrTiO_3$ for cross-validation. Experiments presented in this figure are performed at room temperature under vacuum conditions (10^{-7} mbar) with the same probe tips.

To make sure that we do not have *large clusters* of carbon contamination on the surface, we conducted high-resolution surface characterization with FM-AFM measurements (Figure S3). We imaged the surface area (Figure S3a) that we performed our time-resolved AFM measurements (Figure S3b). We simultaneously recorded the energy dissipation of the cantilever beam. The absence of contrast in the dissipation channel reveals that the surface (that we conducted our experiments) is free of *large clusters* of contaminants and clusters of the segregation of highly nonstoichiometric surface layers[16-21]. The histogram analysis of surface topography shows two different features, the peak is at 0.6 nm with a kink at 0.4 nm height. This implies that the surface has a unit-cell step height (0.4 nm) and fractional step heights of 0.2 nm and 0.6 nm. Non-integer step heights are typically attributed to terminating the crystal both with SrO and TiO_2 layers of the perovskite structure[2, 19, 22]. Besides, surface topography illustrates structures with corners (Figure S3a region I and II) that are attributed to TiO_2 termination and curved features (Figure S3a region III and IV) that are linked to the SrO surface termination[2, 22]. We performed a fast Fourier transfer (FFT) analysis around these areas for cross-validation of this step-edge shape assessment. For regions I and II, we observed 4-fold symmetry in our FFT analysis, which is an indication of cornered structures. However, FFT analysis of regions III and IV did not reveal any 4-fold symmetry, which implies the absence of cornered structures.

We superimposed the time constant measurements with the topography of the surface. The correlation between the topography hints that the longer time constants concentrated around step edges across the surface. We quantified this correlation as a function of distance from step edges. The time constants of measurement points within 25 nm proximity to a step edge (554 ± 31 ms) is larger compared to the time constants of measurement points that are 50 nm or farther from the step edges (383 ± 23 ms). This statistical difference suggests that the local variation in the surface structure and the coordination number of nearby surface atoms may influence the time constants associated with the motion of oxygen vacancies due to the external electric field. Although our results may imply the variation of time constants as a function of the distance from step edges, the exact nature of this variation can only be discerned by conducting atomic-resolution time-resolved measurements across step edges which is beyond the scope of this work. In addition, the surface structures, terminations, internal dislocations, and other defects are potential contributing sources to the variation of time constants associated with vacancy migration. However, exploring all these contributions factors and their potential weight is not possible experimentally and computationally with current experimental and computational methods.

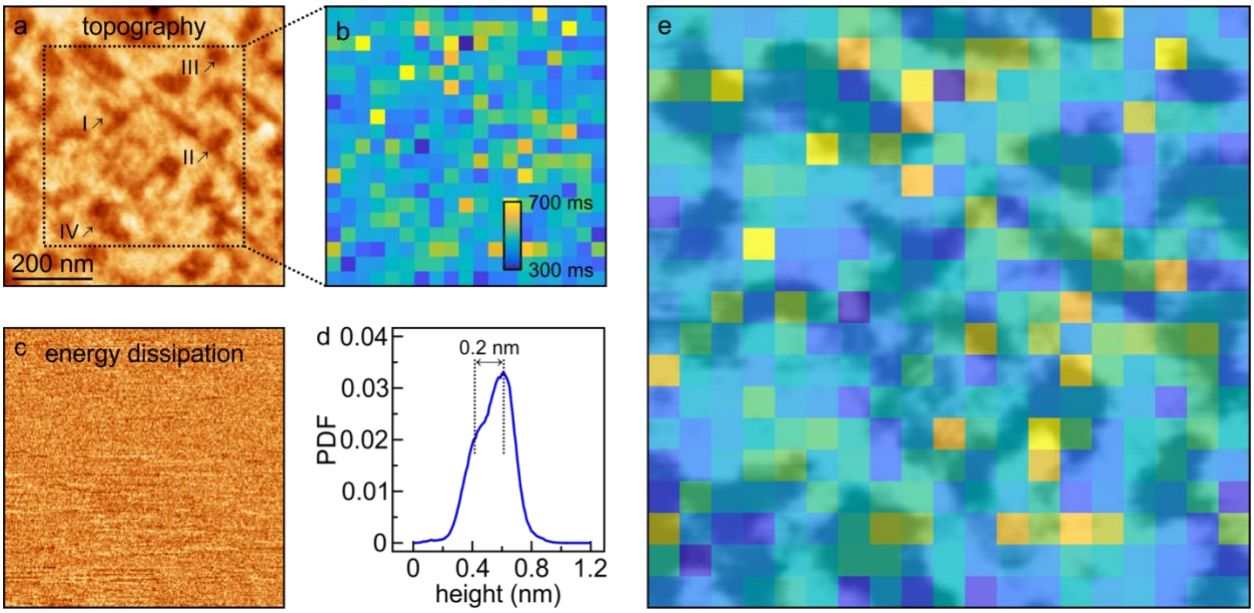

Figure S3. High-resolution characterization of the surface with frequency-modulation based atomic force microscopy. (a-b) Surface topography is measured for the area that we conducted our time-resolved experiments. (c) The energy dissipation is presented by the excitation voltage of the cantilever and changes less than 1% across the scan frame. This small variation in the energy dissipation channel reveals that the surface is free of contaminants or clusters of defects. (d) Histogram analysis of the surface topography shows that the surface has unit-cell and fractional

unit-cell step heights. (e) Superposition of measured time constants with the surface topography reveals that the longer time constants are associated around step edges. This implies that the migration of oxygen vacancies is linked to the variations of local surface topography and stoichiometry.

V. Additional Experimental Data for Pulse Experiments

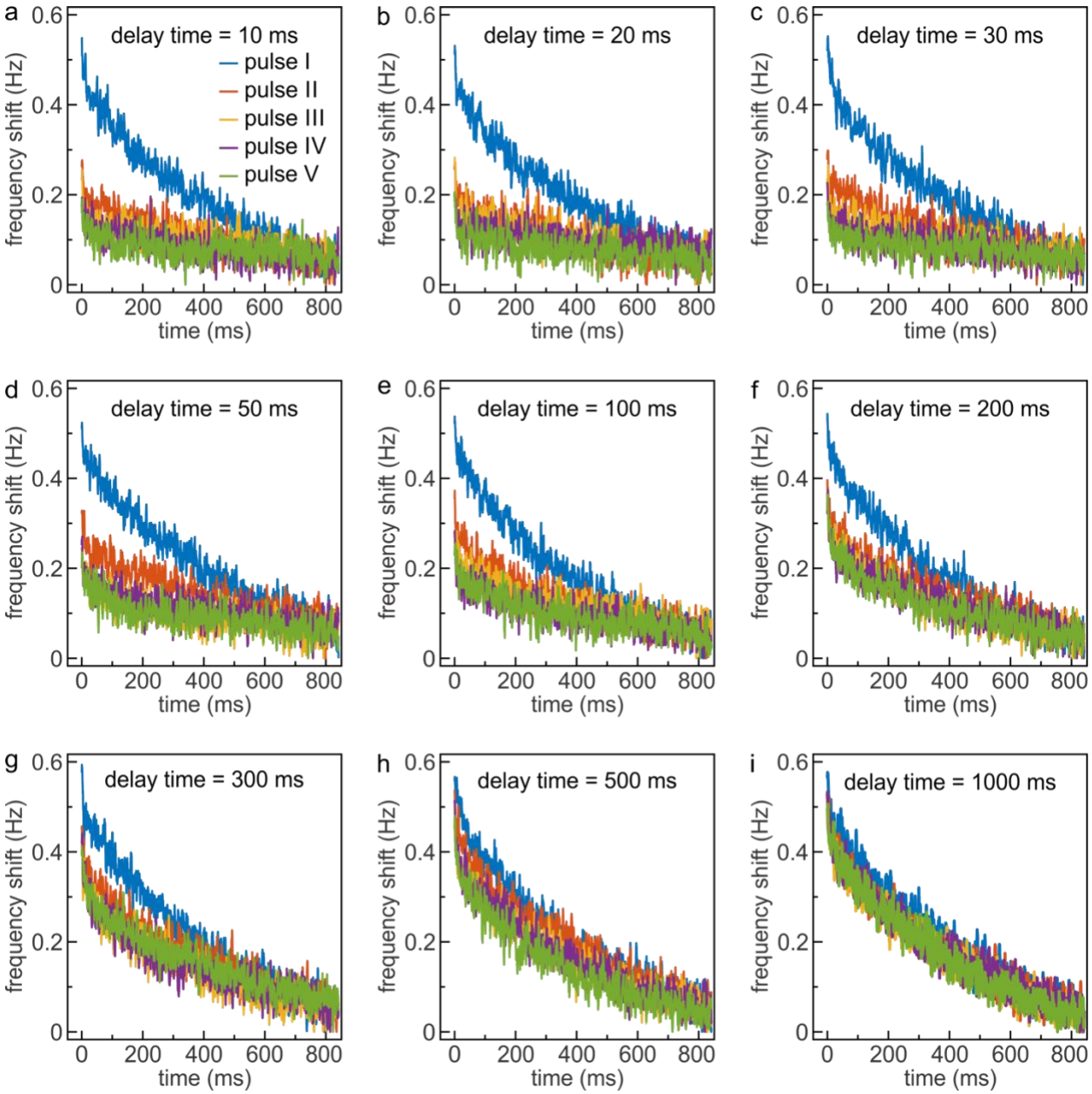

Figure S4. Additional experimental data for the measurement of the time constant of charge carriers with different delay times between pulses. (a-i) The delay time between the time constant is increased from 10 ms to 1000 ms for 5 successive pulses.

VI. First-Principles Calculations

VI a. The Migration Barrier Calculations

Density functional theory (DFT) calculations were performed on a $4 \times 4 \times 4$ $SrTiO_3$ supercell containing 320 atoms in the cubic $Pm\bar{3}m$ perovskite structure (*see Section* VII *below for details*). We focused on addressing the impact of the vacancy concentration upon their migration barriers, as earlier hybrid-functional calculations (in smaller supercells) have indicated that the formation oxygen vacancies is much more thermodynamically favorable compared to other point defects[25].

Oxygen vacancies in perovskites can be either neutral or charged[23-27]. To this end, both the charged and neutral states of oxygen vacancies in $SrTiO_3$ have been studied through first-principles calculations[23-27]. There are three charge states that oxygen vacancies may acquire in $SrTiO_3$: the neutral state, +1 state, and +2 state (denoted as V_O, V_O^+, V_O^{2+} respectively). Figure S5 summarizes the results of *ab-initio* calculations for the formation energy, migration barriers, and charge localization properties which vary amongst these three charge states. As Figure S5a shows, the conduction band minimum is located at 2.13 eV above the valence band maximum according to our calculations. Also, Figure S5b reveals that the formation energy for V_O, V_O^+, V_O^{2+} as a function of the Fermi-level (these results are in good agreement with earlier hybrid-functional calculations in smaller supercells[25]). Our calculations of the formation energy as a function of Fermi-level indicates that V_O^{2+} is the most stable state for Fermi level positions up to 2.24 eV above the valence band minimum. For this reason, as the Fermi-level resides at 2.13 eV, V_O, V_O^+ are less energetically favorable than V_O^{2+}. This is also supported by our experimental measurements, as our sample $SrTiO_3$ is not electrically conductive. The nonconductivity of our samples further implies a Fermi level well below the conduction band minimum (i.e., less than 2.13 eV). Hence, comparison with Figure S5b implies that V_O^{2+} is the most likely vacancy state for the studied samples. Thus, we only focus upon V_O^{2+} defects in our vacancy migration calculations. Figure S5c demonstrates the migration path we used to calculate the migration barriers of an isolated oxygen vacancy in a $4 \times 4 \times 4$ supercell and Figure S5d shows the different migration barriers for oxygen vacancies with different charge states.

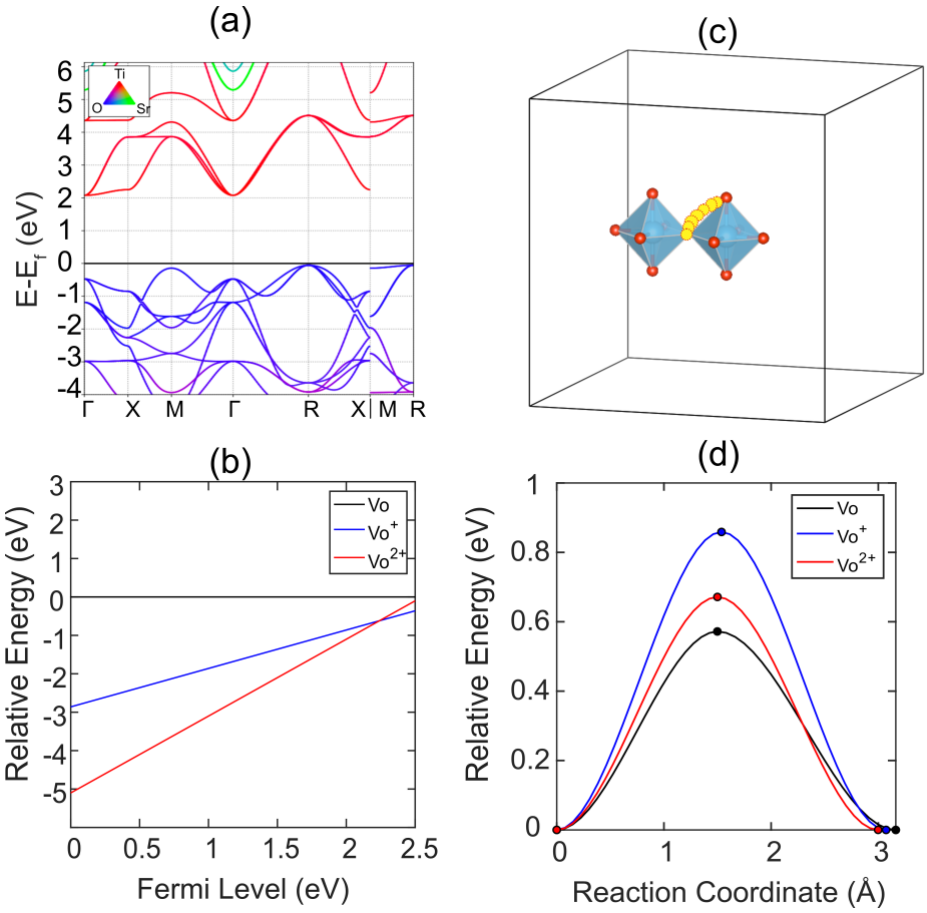

Figure S5. $SrTiO_3$ first-principles calculations including the formation energy and associated properties of oxygen vacancies. (a) Electronic band structure of pristine $SrTiO_3$ (b) Relative formation energy as a function of Fermi level for oxygen vacancy defects in $SrTiO_3$. (c) Oxygen vacancy migration path in a 4×4×4 supercell (only two adjacent TiO_6 polyhedral in the supercell are shown for illustrative purposes). (d) Single vacancy migration barriers for V_O, V_O^+ and V_O^{2+}, respectively.

Our study of V_O^{2+} interactions begins with a consideration of energetically favorable paired vacancy configurations in $4 \times 4 \times 4$ $SrTiO_3$ supercells. We considered the most commonly discussed configurations following the former literature[28], as well as new additional configurations. Figure S6a shows di-vacancy configurations studied. Figure S6b summarizes the relative formation energy interaction of the proposed vacancy-vacancy interactions versus their separation distance. Note the calculations presented in Figure S6b do not include periodic charged supercell corrections, as the first-order charged supercell correction is identical for all configurations in Figure S6 as discussed in Ref.[29] and we are examining their relative formation energy (not total formation energy). This was also done for the kinetic barrier calculations in Figure S7. However, the calculations in Figure S5 must include all the necessary periodic charged

supercell caculations discussed in Refs. [29, 30] as we are comparing the formation of different charge states in Figure S5 and the variationof the bulk/reservoir Fermi-level relative to these charge states. Our calculations reveal that the configuration C in Figure S6a is the most energetically favorable case. For this reason, we selected configuration C to further explore the impact of vacancy interactions on the overall migration process.

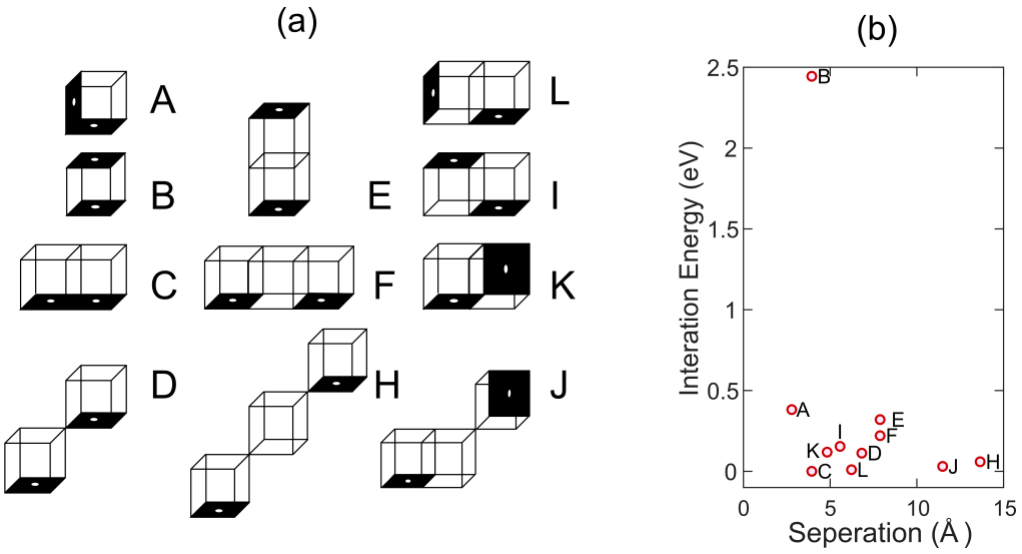

Figure S6. Ab-initio calculations exploring the energetically most favorable states of paired V_O^{+2} vacancies, (a) shows different configurations of vacancies. Each cube represents a $SrTiO_3$ unit cell. The shaded area with an empty circle indicates the location of a V_O^{+2} vacancy. (b) reveals the vacancy-vacancy interaction energies versus their separation distance. Our ab-initio calculations indicate that configuration C energetically is the most favorable configuration.

We employed the climbing image nudged elastic band (CI-NEB) method to compute migration barriers of vacancies[31]. As Figure S7a shows, we first considered the computed energy barrier of 0.67 eV for an isolated V_O^{2+} migrating to its neighboring site in a $4 \times 4 \times 4$ supercell. We compared this energy with the proposed migration path for configuration C depicted in Figure S7b. The migration path corresponds to hopping between C-L-F-L-C configurations (the interaction energy of all such configurations are shown in Figure S6b). The migration barriers between C-L was determined to be 0.45 eV, while the migration barriers between L-F was found to be 0.87 eV. For this reason, the proposed migration pathway in configuration C leads to a larger kinetic barrier to vacancy migration if the vacancy-vacancy system is perturbed from its lowest, the most favorable energy configuration.

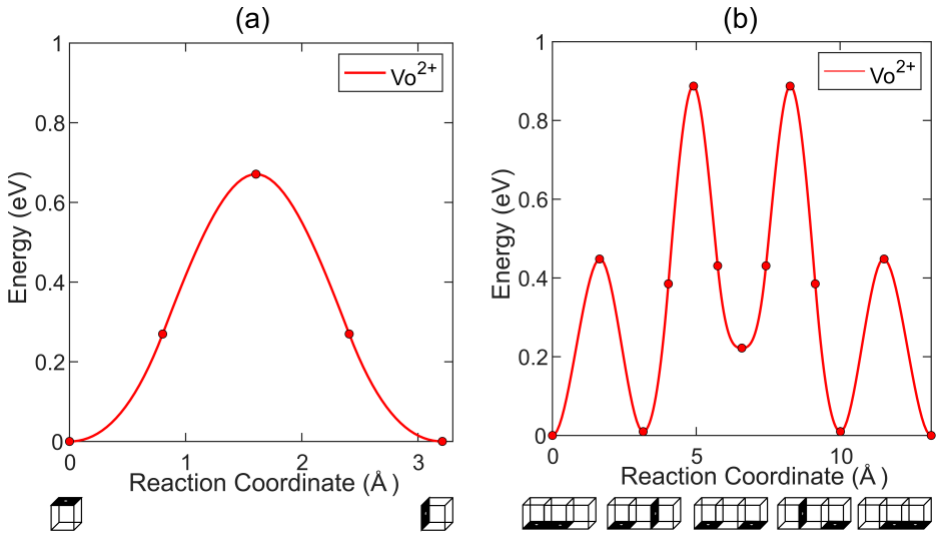

Figure S7. The calculation of migration path barriers. (a) shows the migration barriers of a single V_O^{2+} vacancy. (b) reveals that the proposed migration pathway and computed barriers for V_O^{2+} divacancies with configuration C. All energy barriers were calculated using the climbing image nudged elastic band method with U = 4.36 eV[31].

We hypothesize that amongst the statistical ensemble of configurations that are occupied in vacancy migration, similar interactions obstruct vacancy motion and give rise to a larger overall migration barrier at higher vacancy concentrations. These vacancies that are initially dilute can be clustered closely together by an externally applied field (e.g., via a scanned probe). Even though, it is not possible to compute all such interactions and kinetic barriers of different vacancy configurations, orientations and configurations, our calculations lend first-principles support to our hypothesis and are complementary to the observed experimental results.

VI b. Deformation of the Sample Due to the Tip-sample Interaction

The existence of the AFM probe and applied bias voltage between the tip and the sample results in a tip-sample interaction force. This tip-sample interaction force may deform the sample locally. For this reason, we also investigated the effect of sample deformation on the migration barrier. To this end, the bulk modulus of $SrTiO_3$ calculated utilizing the Perdew-Burke-Ernzerhof (PBE) functional[32] was determined to be 172 GPa, which agrees well with previous DFT studies[33] and the experimental value of 174 GPa[34]. The tip is located at a distance of 20 nm during experiments. Due to this reason, the tip has an effective tip-sample interaction area 20 nm in radius. The conversion of resonance frequency shift data to the tip-sample interaction force shows that the total

tip-sample force is on the order of 3 nN. This tip-sample interaction force will lead to a local pressure of 0.0024 GPa. This amount of force that will deform the lattice by approximately 0.00011 nm. For this reason, the deformation due to the tip-sample interaction force is negligible and has no effect on the migration barrier of oxygen vacancies.

VII. First-Principles Methodology

All first-principles calculations were performed within the Vienna Ab initio Simulation Package (VASP)[35-38] utilizing the PBE functional[32]. We utilized projector augmented wave (PAW) potentials[39, 40] of the form: Sr($4s^2 4p^6 5s^2$), Ti($3p^6 4s^2 3d^2$), O($2s^2 2p^4$). All calculations were spin polarized. The pristine unit cell of $SrTiO_3$ was fully relaxed using the PBE functional with a $7 \times 7 \times 7$ Monkhorst–Pack[41] k-point grid and a plane-wave energy cut-off of 650 eV. The interatomic forces were converged to less than 0.01 eV/ Å. This results in a lattice parameter of 3.940 Å in good agreement with the experimental value of 3.905 Å[42]. We did not use DFT+U to further optimize the lattice parameter, as it leads to a greater deviation from the experimental lattice parameter. Band gap and lattice parameter variation as a function of the U value in VASP can be found in Figure S8. Through detailed inquires, we have found that vacancy interactions in the $4 \times 4 \times 4$ supercell range can sometimes lead to a sustained, long-range octahedral tilting across the entire supercell, when structural converge is set below 0.05 eV/ Å. We believe that this is an artifact of the supercell method which sometimes misrepresents the true interaction of vacancies in a mesoscopic system due to the limited dimensions of the supercell used. For this reason, we ended configurations subject to such long-range distortions at a higher total energy before they could be reached. To avoid this unphysical distortion of the periodic supercell, we obtained at a lower convergence criterion (0.05 eV/ Å) for C, D, L, K configurations presented in Figure S6. To verify that the long-range octahedral distortions are a supercell size artifact, and not a convolved lattice parameter error, we relaxed both the lattice constant and defect configuration simultaneously for configuration L at the chosen U value discussed below (detailed run files can be found amongst our Supporting data). Again, with these self-consistently relaxed unit cells, the same long-range octahedral distortions are still obtained. Larger supercell sizes are beyond our computational capabilities (even the presented calculations were quite computationally demanding). The removal of long-range octahedral distortions should be explored in larger supercells in future work as computational algorithms improve.

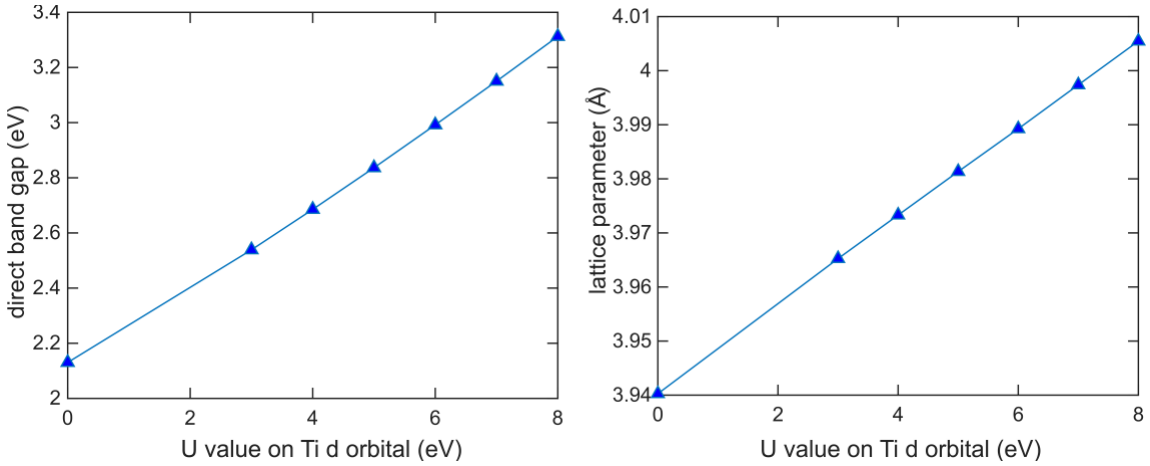

Figure S8. $SrTiO_3$ band gap and lattice constant as a function of the U value projected on Ti d-orbitals in VASP.

For all supercell calculations involving oxygen vacancies and divacancies, we employed the DFT+U approach[43] with an effective Hubbard U parameter set at 4.36 eV[27, 28, 44, 45] on the Ti d-orbitals. The U term is needed to correct the on-site Coulomb interaction of Ti 3d orbitals[27, 28, 44, 45]. This U value is commonly used in first-principles studies of $SrTiO_3$[27, 28, 44, 45] and the overall single oxygen vacancy properties calculated with this U value are arguably comparable to hybrid functional results[25]. We obtained a calculated band gap of 2.13 eV with this U value, which lies below the known experimental band gap of 3.25 eV[46]. By employing the generalized form of Koopmans' theorem[47-49] one might better estimate the U value. Nevertheless, the 4.36 eV U value we employed enables direct comparison with previous first-principles studies of $SrTiO_3$[27, 28, 44, 45]. All our vacancy results were obtained in $4 \times 4 \times 4$ STO supercells sampled via a $2 \times 2 \times 2$ Monkhorst–Pack[41] k-point grid. The element-decomposed electronic band structure of $SrTiO_3$ was plotted using pymatgen[50]. The migration path of oxygen vacancy was visualized through VESTA[51]. The formation energies of the oxygen vacancies were calculated following the procedure discussed elsewhere[25, 30], while utilizing the finite size and charged supercell correction scheme[30]. The reader is referred to Refs.[29, 30] for details concerning these important defect energy corrections. Hybrid functionals were considered far too computationally costly for such a large system, compounded with the challenge of many coupled nudged elastic band lattice calculations.

VIII. Relation Between the Activation Energy and Diffusion

For a vacancy moving in the bulk of a material, we can write the diffusion coefficient using Einstein's relation for a random walk[52],

$$D = \frac{<\Delta r^2>}{2\alpha t} \tag{6}$$

where $< \Delta r^2 >= Nl^2$ is the mean-square displacement of the diffusing particle, α is dimensionality of the process, and t is the duration over which the diffusion is observed. Here, N is the number of jumps and l is the jump length. The number of jumps can also be written as:

$$N = n\Gamma t, \tag{7}$$

In equation 7, n is the number of nearest neighbors and models the number of jump-equivalent directions available to the vacancy and Γ is the hopping rate. The hopping rate can be further expressed as[53]:

$$\Gamma \approx \frac{k_B T}{h} e^{\frac{-\Delta F}{k_B T}} \tag{8}$$

In equation 8, ΔF is the free energy change between the top of the kinetic barrier and the vacancy in its equilibrium position, k_B is Boltzmann constant, h is Plank's constant and T is the system temperature. The free energy change has both total energy and entropic contributions and can be written in the form[54]:

$$\Delta F = \Delta E - T\Delta S. \tag{9}$$

In equation 9, ΔE is the activation energy barrier of diffusion ($\Delta E = E_a$) and ΔS is the vibrational entropy. Since we want to approximate the vacancy mobility, we can assume that during the hopping process the change in the local vibrational frequency is negligible in comparison with vibrational frequency in the initial state. As we are not considering high temperatures (i.e. thousands of degrees), this is a reasonable assumption[55]. As a result, we can write:

$$\Delta S = \Delta S_{vib} \cong 0. \tag{10}$$

In most calculations of vacancy diffusion in crystalline materials at low temperatures, ΔS is assumed to be zero[56].

If equation 6 is rewritten by substituting equation 7:

$$D = \frac{n\Gamma t l^2}{2\alpha t} = \frac{n\Gamma l^2}{2\alpha}. \tag{11}$$

Substituting equation 8 in equation 11, leads to:

$$D = \frac{k_B T n l^2}{h \quad 2\alpha} \exp\left(\frac{\Delta S}{k_B T}\right) \exp\left(\frac{-E_a}{k_B T}\right). \tag{12}$$

As the next step, substituting equation 10 in equation 12 results:

$$D = \frac{k_B T n l^2}{h \quad 2\alpha} \exp\left(\frac{-E_a}{k_B T}\right). \tag{13}$$

Finally, from Einstein's diffusion relation[52] we can arrive at the mobility μ via:

$$\mu = \frac{q}{k_B T} D \tag{14}$$

In Equation 14, q is the charge of the vacancy. From this vacancy mobility and the diffusion energy barrier can be related inserting equation 13 in equation 14:

$$\mu = \frac{q n l^2}{2\alpha h} \exp\left(\frac{-E_a}{k_B T}\right) \tag{15}$$

Note that *l* refers to the hop distance between vacancy configurations, for example the distance the vacancy in Figure 1 would move from its current site to a nearest neighbor oxygen site when migrating. Equation 15 reveals that an increase in the bulk activation barrier will decrease the mobility of vacancies – or, conversely, how the mobility may be computed from the activation barrier.

IX. Additional Experimental Data for the Spatial Extent of Temporal Correlations

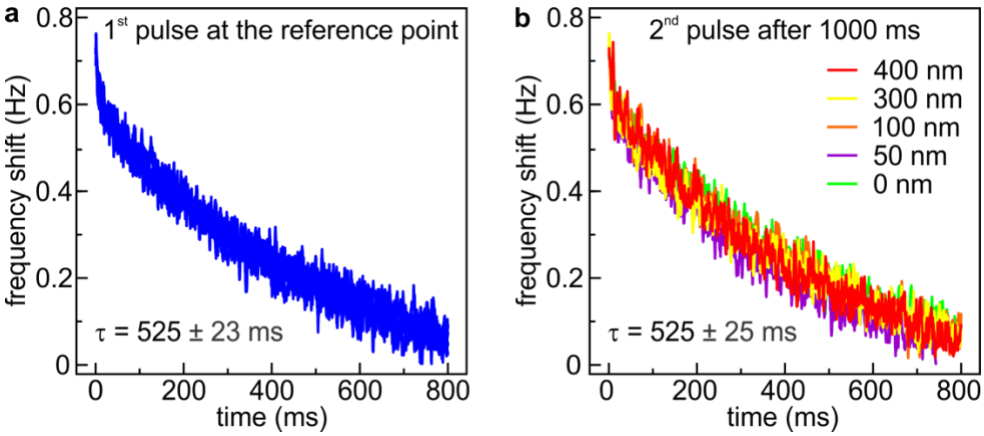

Figure S9. Additional data for the measurement of the spatial extent of nonergodic dynamics. (a) shows the decay of the frequency shift for the first pulse of the reference point for five successive experiments. This result demonstrates that there is no tip or sample modification between experiments. (b) is the measurement of the time constant at various distances after waiting for 1000 ms. This demonstrates that the time constant associated at each point is very similar and within the experimental uncertainty in the absence of temporal correlations.

References for Supporting Information

1. Chambers, S. A.; Droubay, T. C.; Capan, C.; Sun, G. Y., Unintentional F doping of $SrTiO_3$(001) etched in HF acid-structure and electronic properties. *Surface Science* **2012,** *606* (3), 554-558.

2. Dagdeviren, O. E.; Simon, G. H.; Zou, K.; Walker, F. J.; Ahn, C.; Altman, E. I.; Schwarz, U. D., Surface phase, morphology, and charge distribution transitions on vacuum and ambient SrTiO3(100). *Physical Review B* **2016,** *93* (19), 195303.

3. Zahl, P.; Bierkandt, M.; Schröder, S.; Klust, A., The flexible and modern open source scanning probe microscopy software package GXSM. *Review of Scientific Instruments* **2003,** *74* (3), 1222-1227.

4. Albrecht, T. R.; Grutter, P.; Horne, D.; Rugar, D., Frequency modulation detection using high-Q cantilevers for enhanced force microscope sensitivity. *Journal of Applied Physics* **1991,** *69*.

5. Schirmeisen, A.; Taskiran, A.; Fuchs, H.; Roling, B.; Murugavel, S.; Bracht, H.; Natrup, F., Probing ion transport at the nanoscale: Time-domain electrostatic force spectroscopy on glassy electrolytes. *Applied Physics Letters* **2004,** *85* (11), 2053-2055.

6. Schirmeisen, A.; Taskiran, A.; Bracht, H.; Roling, B., Ion Jump Dynamics in Nanoscopic Subvolumes Analyzed by Electrostatic Force Spectroscopy. *Zeitschrift für Physikalische Chemie* **2010,** *224*, 1831-1852.

7. Taskiran, A.; Schirmeisen, A.; Fuchs, H.; Bracht, H.; Roling, B., Time-domain electrostatic force spectroscopy on nanostructured lithium-ion conducting glass ceramics: analysis

and interpretation of relaxation times. *Physical Chemistry Chemical Physics* **2009,** *11* (26), 5499-5505.

8. Schirmeisen, A.; Taskiran, A.; Fuchs, H.; Bracht, H.; Murugavel, S.; Roling, B., Fast Interfacial Ionic Conduction in Nanostructured Glass Ceramics. *Physical Review Letters* **2007,** *98* (22), 225901.

9. Mascaro, A.; Wang, Z.; Hovington, P.; Miyahara, Y.; Paolella, A.; Gariepy, V.; Feng, Z.; Enright, T.; Aiken, C.; Zaghib, K.; Bevan, K. H.; Grutter, P., Measuring Spatially Resolved Collective Ionic Transport on Lithium Battery Cathodes Using Atomic Force Microscopy. *Nano Letters* **2017,** *17* (7), 4489-4496.

10. Ngai, K. L.; Wang, Y. N.; Magalas, L. B., Theoretical basis and general applicability of the coupling model to relaxations in coupled systems. *Journal of Alloys and Compounds* **1994,** *211-212*, 327-332.

11. Funke, K., Jump relaxation in solid electrolytes. *Progress in Solid State Chemistry* **1993,** *22* (2), 111-195.

12. Ngai, K. L.; Kanert, O., Comparisons between the coupling model predictions, Monte Carlo simulations and some recent experimental data of conductivity relaxations in glassy ionics. *Solid State Ionics* **1992,** *53-56*, 936-946.

13. Arrhenius, S., Über die Dissociationswärme und den Einfluss der Temperatur auf den Dissociationsgrad der Elektrolyte. In *Zeitschrift für Physikalische Chemie*, 1889; Vol. 4U, p 96.

14. Arrhenius, S., Über die Reaktionsgeschwindigkeit bei der Inversion von Rohrzucker durch Säuren. In *Zeitschrift für Physikalische Chemie*, 1889; Vol. 4U, p 226.

15. Mascaro, A. Development of Scanning Probe Microscopy Techniques for the Study of Lithium Ion Battery Materials. McGill University, Montreal, Canada, 2015.

16. Garcia, R., *Amplitude Modulation Atomic Force Microscopy*. Wiley-VCH: Singapore, 2010.

17. Giessibl, F. J., Advances in atomic force microscopy. *Reviews of Modern Physics* **2003,** *75* (3), 949-983.

18. Liang, Y.; Bonnell, D. A., Atomic structures of reduced $SrTiO_3$(001) surfaces. *Surface Science Letters* **1993,** *285* (3), L510-L516.

19. Newell, D. T.; Harrison, A.; Silly, F.; Castell, M. R., $SrTiO_3$(001)−($\sqrt{5}\times\sqrt{5}$)−R26° reconstruction: A surface resulting from phase separation in a reducing environment. *Physical Review B* **2007,** *75* (20), 205429.

20. Tilley, R. J. D., An electron microscope study of perovskite-related oxides in the Sr□Ti□O system. *Journal of Solid State Chemistry* **1977,** *21* (4), 293-301.

21. Brooks, C. M.; Wilson, R. B.; Schäfer, A.; Mundy, J. A.; Holtz, M. E.; Muller, D. A.; Schubert, J.; Cahill, D. G.; Schlom, D. G., Tuning thermal conductivity in homoepitaxial $SrTiO_3$ films via defects. *Applied Physics Letters* **2015,** *107* (5), 051902.

22. Kubo, T.; Nozoye, H., Surface structure of $SrTiO_3$(100). *Surface Science* **2003,** *542* (3), 177-191.

23. Al-Hamadany, R.; Goss, J. P.; Briddon, P. R.; Mojarad, S. A.; O'Neill, A. G.; Rayson, M. J., Impact of tensile strain on the oxygen vacancy migration in $SrTiO_3$: Density functional theory calculations. *Journal of Applied Physics* **2013,** *113* (22).

24. Buban, J. P.; Iddir, H.; Öğüt, S., Structural and electronic properties of oxygen vacancies in cubic and antiferrodistortive phases of $SrTiO_3$. *Physical Review B - Condensed Matter and Materials Physics* **2004,** *69* (18), 3-6.

25. Janotti, A.; Varley, J. B.; Choi, M.; Van de Walle, C. G., Vacancies and small polarons in $SrTiO_3$. *Physical Review B* **2014,** *90* (8), 085202-085202.

26. Mitra, C.; Lin, C.; Robertson, J.; Demkov, A. A., Electronic structure of oxygen vacancies in $SrTiO_3$ and $LaAlO_3$. *Physical Review B* **2012,** *86* (15), 155105-155105.

27. Zhang, L.; Liu, B.; Zhuang, H.; Kent, P. R. C.; Cooper, V. R.; Ganesh, P.; Xu, H., Oxygen vacancy diffusion in bulk $SrTiO_3$ from density functional theory calculations. *Computational Materials Science* **2016,** *118*, 309-315.

28. Cuong, D. D.; Lee, B.; Choi, K. M.; Ahn, H.-S.; Han, S.; Lee, J., Oxygen Vacancy Clustering and Electron Localization in Oxygen-Deficient $SrTiO_3$: LDA+U Study. *Phys. Rev. Lett.* **2007,** *98* (11), 115503-115503.

29. Kumagai, Y.; Oba, F., Electrostatics-based finite-size corrections for first-principles point defect calculations. *Physical Review B* **2014,** *89* (19), 195205.

30. Lany, S.; Zunger, A., Assessment of correction methods for the band-gap problem and for finite-size effects in supercell defect calculations: Case studies for ZnO and GaAs. *Physical Review B* **2008,** *78* (23), 235104.

31. Henkelman, G.; Uberuaga, B. P.; Jónsson, H., A climbing image nudged elastic band method for finding saddle points and minimum energy paths. *The Journal of Chemical Physics* **2000,** *113* (22), 9901-9904.

32. Perdew, J. P.; Burke, K.; Ernzerhof, M., Generalized Gradient Approximation Made Simple. *Physical Review Letters* **1996,** *77* (18), 3865-3868.

33. Piskunov, S.; Heifets, E.; Eglitis, R. I.; Borstel, G., Bulk properties and electronic structure of $SrTiO_3$, $BaTiO_3$, $PbTiO_3$ perovskites: an ab initio HF/DFT study. *Computational Materials Science* **2004,** *29* (2), 165-178.

34. Bell, R. O.; Rupprecht, G., Elastic Constants of Strontium Titanate. *Physical Review* **1963,** *129* (1), 90-94.

35. Kresse, G.; Furthmüller, J., Efficient iterative schemes for ab initio total-energy calculations using a plane-wave basis set. *Physical Review B* **1996,** *54* (16), 11169-11186.

36. Kresse, G.; Furthmüller, J., Efficiency of ab-initio total energy calculations for metals and semiconductors using a plane-wave basis set. *Computational Materials Science* **1996,** *6* (1), 15-50.

37. Kresse, G.; Hafner, J., Ab initio molecular dynamics for liquid metals. *Physical Review B* **1993,** *47* (1), 558-561.

38. Kresse, G.; Hafner, J., Ab initio molecular-dynamics simulation of the liquid-metalamorphous- semiconductor transition in germanium. *Physical Review B* **1994,** *49* (20), 14251-14269.

39. Blöchl, P. E., Projector augmented-wave method. *Physical review B* **1994,** *50* (24), 17953.

40. Kresse, G.; Joubert, D., From ultrasoft pseudopotentials to the projector augmented-wave method. *Physical review b* **1999,** *59* (3), 1758.

41. Monkhorst, H. J.; Pack, J. D., Special points for Brillouin-zone integrations. *Phys. Rev. B* **1976,** *13* (12), 5188-5192.

42. Schmidbauer, M.; Kwasniewski, A.; Schwarzkopf, J., High-precision absolute lattice parameter determination of $SrTiO_3$, $DyScO_3$ and $NdGaO_3$ single crystals. *Acta Crystallographica Section B* **2012,** *68* (1), 8-14.

43. Liechtenstein, A. I.; Anisimov, V. I.; Zaanen, J., Density-functional theory and strong interactions: Orbital ordering in Mott-Hubbard insulators. *Physical Review B* **1995,** *52* (8).

44. Brown, J. J.; Ke, Z.; Geng, W.; Page, A. J., Oxygen Vacancy Defect Migration in Titanate Perovskite Surfaces: Effect of the A-Site Cations. *The Journal of Physical Chemistry C* **2018,** *122* (26), 14590-14597.

45. Jeschke, H. O.; Shen, J.; Valentí, R., Localized versus itinerant states created by multiple oxygen vacancies in $SrTiO_3$. *New Journal of Physics* **2015,** *17* (2), 023034-023034.

46. van Benthem, K.; Elsässer, C.; French, R. H., Bulk electronic structure of $SrTiO_3$: Experiment and theory. *Journal of Applied Physics* **2001,** *90* (12), 6156-6164.

47. Janak, J. F., Proof that $\partial E \partial ni = \varepsilon$ in density-functional theory. *Physical Review B* **1978,** *18* (12), 7165-7168.

48. Lany, S.; Zunger, A., Polaronic hole localization and multiple hole binding of acceptors in oxide wide-gap semiconductors. *Physical Review B* **2009,** *80* (8), 085202-085202.

49. Perdew, J. P.; Parr, R. G.; Levy, M.; Balduz, J. L., Jr., DFT for Fractional Particle Number: Derivative Discontinuity. *Physical Review Letters* **1982,** *49* (23), 1691-1691.

50. Ong, S. P.; Richards, W. D.; Jain, A.; Hautier, G.; Kocher, M.; Cholia, S.; Gunter, D.; Chevrier, V. L.; Persson, K. A.; Ceder, G., Python Materials Genomics (pymatgen): A robust, open-source python library for materials analysis. *Computational Materials Science* **2013,** *68*, 314-319.

51. Momma, K.; Izumi, F., VESTA 3 for three-dimensional visualization of crystal, volumetric and morphology data. *Journal of Applied Crystallography* **2011,** *44* (6), 1272-1276.

52. Einstein, A., Über die von der molekularkinetischen Theorie der Wärme geforderte Bewegung von in ruhenden Flüssigkeiten suspendierten Teilchen. *Annalen der Physik* **1905,** *322* (8), 549-560.

53. Vineyard, G. H., Frequency factors and isotope effects in solid state rate processes. *Journal of Physics and Chemistry of Solids* **1957,** *3* (1-2), 121-127.

54. Antczak, G.; Ehrlich, G., *Surface diffusion: metals, metal atoms, and clusters*. Cambridge University Press: 2010.

55. Maier, J., *Physical chemistry of ionic materials: ions and electrons in solids*. John Wiley & Sons: 2004.

56. Kürpick, U.; Kara, A.; Rahman, T. S., Role of lattice vibrations in adatom diffusion. *Physical review letters* **1997,** *78* (6), 1086.